



# AuPd/C core-shell and alloy nanoparticles with enhanced catalytic activity toward the electro-oxidation of ethanol in alkaline media

Lays S.R. Silva<sup>a,b</sup>, Caio V.S. Almeida<sup>a,b</sup>, Cristiano T. Meneses<sup>c</sup>, Elizete A. Batista<sup>d</sup>, Sydney F. Santos<sup>e</sup>, Katlin I.B. Eguiluz<sup>a,b</sup>, Giancarlo R. Salazar-Banda<sup>a,b,\*</sup>

<sup>a</sup> Laboratory of Electrochemistry and Nanotechnology, Institute of Technology and Research, 49.032-490, Aracaju, SE, Brazil

<sup>b</sup> Process Engineering Postgraduate Program, Tiradentes University, 49.032-490, Aracaju, SE, Brazil

<sup>c</sup> Department of Physics, Universidade Federal de Sergipe, Campus Itabaiana, Av. Marechal Rondon, Aracaju, SE, Brazil

<sup>d</sup> Department of Physical Chemistry, Institute of Chemistry, Universidade Estadual Paulista, Campus Araraquara, Av. Araraquara-Jatú, Araraquara, SP, Brazil

<sup>e</sup> Center of Engineering, Modeling, and Applied Social Sciences, Universidade Federal do ABC, Av. dos Estados 5001, Santo André, SP, Brazil

## ARTICLE INFO

### Keywords:

Core-shell nanostructures  
PdAu-based electrocatalysts  
Ethanol electro-oxidation  
Scanning-transmission electron microscopy  
Fuel cells

## ABSTRACT

Carbon-supported Pd, Au@Pd core-shell and Au<sub>1-x</sub>Pd<sub>x</sub>-alloyed nanoparticles were prepared by a chemical reduction method and characterized by different experimental techniques, including X-ray powder diffraction, transmission electron microscopy, scanning-transmission electron microscopy using bright-field and high-angle annular dark field detectors and X-ray energy dispersive spectroscopy. The catalytic mass activity toward ethanol oxidation was assessed by cyclic voltammetry and chronoamperometry at room temperature. The measurements showed that the addition of Au enhances remarkably the electrocatalytic activity of the material, due to the bifunctional effect of Au<sub>1-x</sub>Pd<sub>x</sub>/C alloys, and the synergetic effect on Au@Pd/C, resulting in a dissolution resistance of core-shell catalysts at potentials of 1.5 V versus reversible hydrogen electrode. In situ Fourier transform infrared spectroscopy measurements showed that the mechanism for ethanol oxidation depends on the electrocatalyst structure and morphology. Acetate was identified as the main product of ethanol electro-oxidation on the studied electrocatalysts. However, the presence of a core-shell structure on Au@Pd/C resulted in enhanced ethanol oxidation selectivity toward CO<sub>2</sub>. The improvement of activity is attributed to the interaction between Pd shell and Au core.

## 1. Introduction

In recent years, there has been growing interest in developing technologies for direct ethanol fuel cells (DEFCs) in an alkaline medium [1–4]. The use of ethanol has received great attention because it can easily be produced in large quantities from biological processing of agricultural products and is considered a renewable energy source due to low pollutant emission characteristics [5]. Moreover, ethanol is a strategic fuel because of its low toxicity, since its complete oxidation to CO<sub>2</sub> involves 12 electrons per molecule oxidized, resulting in high energy density (8.01 kW h Kg<sup>-1</sup> or 6.34 kW h L<sup>-1</sup>, b.p. 78.4 °C) when compared to hydrogen [6–8], as well as other alcohols, such as methanol (6.09 kW h Kg<sup>-1</sup>, b.p. 64.7 °C) [9,10], glycerol (5.0 kW h Kg<sup>-1</sup>, b.p. 290.0 °C) [11] and ethylene glycol (5.2 kW h Kg<sup>-1</sup>, b.p. 197.3 °C) [10].

However, the greatest obstacle to the commercialization of DEFCs is the lack of catalysts that can trigger the organic oxidation at a favorable

rate [3]. The search for an active catalyst that yields high current densities during the ethanol oxidation reaction (EOR) is a key goal in research into DEFCs.

Ethanol, being a molecule with two C atoms (C<sub>2</sub>), suffers an additional problem related to the breaking of the C–C bond, which is a prerequisite for the complete oxidation of ethanol to CO<sub>2</sub>. Some poisonous intermediates, such as CO, are generated and are strongly adsorbed on the catalyst surface through the process of electro-oxidation [12,13], blocking active sites for further catalysis. This results in a dramatic decrease in electrochemical activity of the catalyst.

In this context, comprehensive fundamental studies of electro-oxidation of ethanol using Pt catalysts in acidic and basic media are widely reported in the literature [14–22]. Compared to platinum-based catalysts, palladium is widely available and has potential as a platinum substitute for various energy-related reactions in alkaline media. This is because Pd presents superior catalytic activity than that of Pt for ethanol oxidation in this environment [23–30]. These features have

\* Corresponding author at: Laboratory of Electrochemistry and Nanotechnology, Institute of Technology and Research, 49.032-490, Aracaju, SE, Brazil.  
E-mail address: [gianrsb@gmail.com](mailto:gianrsb@gmail.com) (G.R. Salazar-Banda).

<https://doi.org/10.1016/j.apcatb.2019.03.067>

Received 24 October 2018; Received in revised form 12 March 2019; Accepted 25 March 2019

Available online 29 March 2019

0926-3373/ © 2019 Elsevier B.V. All rights reserved.

motivated several fundamental and applied studies on the electrocatalytic behavior of Pd [31–34].

Further, the anti-poisoning and reactivity of Pd-based catalysts can be improved through the formation of bi- and tri-metallic alloys, such as PdNi (oxygen reduction) [13], AuPdPd (methanol oxidation) [24], AuPd (formic acid oxidation) [35,36], PtPdAu (ethanol oxidation) [3] and PdAu (sodium borohydride oxidation) [25].

Another effective method to enhance Pd catalytic activity is through changing the electronic nature and morphology of the Pd surface [37,38]. Bimetallic nanoparticles with a core-shell structure are types of heterogeneous nanomaterial with interesting electrocatalytic behavior. The electronic interaction between the two electron-rich elements and the lattice strain created in the crystalline planes in the shell of these core-shell particles due to the lattice mismatch can modify the electronic properties on the nanoparticle surface [36,39]. In particular, AuPd core-shell nanoparticles have shown enhanced electrochemical activities for some fuel cell oxidation reactions [40–45].

For instance, as demonstrated by Hsu et al. [40], AuPd core-shell nanoparticles exhibit enhanced catalytic activity toward formic acid oxidation. The peak potential and onset potential of formic acid oxidation of the core-shell nanoparticles (0.58 V and 0.14 V, respectively) were more than 60 mV lower than those of the Pd black (0.65 V and 0.2 V). Chronoamperometry tests were used to study the stability of catalytic formic acid oxidation. The prepared Au@Pd nanoparticles exhibit the highest mass-specific current density ( $0.035 \text{ mA } \mu\text{g}^{-1}$ ) in comparison to Pd black ( $0.001 \text{ mA } \mu\text{g}^{-1}$ ). This behavior is a result of changes in the lattice strain, which are induced by lattice mismatch between the Au core and Pd shell. Wang et al. [41] demonstrated that AuPd core-shell nanobricks (CNBs) have enhanced performance toward ethanol electro-oxidation, as a result of the exposed stepped surfaces, high-index facets, and the synergistic effects of the core and shell metals.

Therefore, motivated by previous researches on AuPd electrocatalysts, we studied the influence of AuPd catalyst morphology on the EOR and evaluated the influence of gold content on the AuPd catalysts. Nanostructured AuPd core-shell and alloy catalysts were synthesized, varying the Au content in order to improve the catalytic activity of Pd catalysts toward the EOR.

The series of bimetallic alloy catalysts were synthesized through the simultaneous reduction of metal chlorides (Au and Pd) by  $\text{NaBH}_4$ . Physical characterizations were performed in order to identify the present phases, determine the average particle sizes and investigate the formation of the Au@Pd core-shell nanostructure. The electrochemical activity of the developed catalysts toward ethanol oxidation was studied using electrochemical methods. The EOR byproducts were identified by electrochemical in situ Fourier transform infrared spectroscopy measurements.

## 2. Experimental methods

### 2.1. Synthesis of the catalysts

All carbon-supported AuPd-based catalysts were prepared using a method similar to that reported by Kaplan and coworkers [46]. Briefly, for the synthesis of the Au–Pd core-shell nanoparticles, the Au precursor ( $\text{AuCl}_3 \geq 99.95\%$ , Sigma-Aldrich) was dissolved in a  $0.4 \text{ mol L}^{-1}$  hydrochloric acid solution ( $\text{HCl} \geq 99.95\%$ , Sigma-Aldrich). Later, carbon (Alfa Aesar/Acetylene,  $\geq 99.9\%$ , Johnson Matthey Company) was dispersed in the Au solution and was then subjected to 1 h of ultrasonication. Ammonium hydroxide ( $\text{NH}_4\text{OH}$ , 30%, Vetec<sup>®</sup>) was added dropwise and stirred for 1.5 h at pH 11. Afterwards, an excess of  $0.1 \text{ mol L}^{-1}$  sodium borohydride solution ( $\text{NaBH}_4$ ,  $\geq 98.0\%$ , Sigma-Aldrich) was added rapidly to the mixture, which was then stirred for 4 h. The powder obtained was separated by centrifugation, washed with ultrapure water and dried at  $80^\circ\text{C}$  for 8 h.

In order to synthesize the Pd shell on the Au/C nanoparticles, the

cleaned and dried powder was dispersed into a  $0.4 \text{ mol L}^{-1}$  HCl solution containing appropriate amounts of palladium chloride ( $\text{PdCl}_2$ ,  $\geq 99.0\%$ , Sigma-Aldrich). The reduction of the shell was carried out by the same procedure as used for the core. The resulting powder was recovered and treated as previously described. The  $\text{Au}_{1-x}\text{Pd}_x/\text{C}$  alloy catalysts were synthesized by a similar procedure. A  $0.4 \text{ M HCl} + \text{AuCl}_3 + \text{PdCl}_2$  solution was prepared and the metals were simultaneously reduced onto Alfa Aesar carbon using  $\text{NH}_4\text{OH}$  solution followed by the addition of  $\text{NaBH}_4$ . The molar ratios between Au and Pd were 80:20 for the core-shell catalyst and 10:90, 30:70, 50:50, 70:30 and 80:20 for the alloy catalysts. The total metal loading was kept at 20 wt % for all catalysts.

### 2.2. Physical characterizations

Transmission electron microscopy (TEM), scanning-transmission electron microscopy (STEM) with bright-field (BF) and high-angle annular dark field (HAADF) images were performed on an FEI TECNAI G<sup>2</sup>F20 electron microscope operated at 200 kV. The average size of the nanoparticles was obtained using ImageJ software. Energy dispersive X-ray spectrometry (EDX) coupled to the TEM operating in STEM mode was used to determine the chemical compositions, as well as the elemental distribution in the nanoparticles. For the TEM/STEM measurements, a drop of the nanoparticle solution was dispensed onto a 3-mm carbon-coated copper grid and the sample dried under vacuum at room temperature. Powder X-ray diffraction (XRD) patterns were recorded using a PANalytical Empyrean diffractometer with  $\text{Cu K}\alpha$  radiation ( $\lambda = 0.154178 \text{ nm}$ ) at 40 kV and 40 mA using a PIXcel<sup>1D</sup> detector. The scanning angle ( $2\theta$ ) ranged from  $20^\circ$  to  $80^\circ$  at a scanning rate of  $2^\circ \text{ min}^{-1}$ .

### 2.3. Electrochemical measurements

Electrochemical measurements were carried out in a Pyrex<sup>®</sup> borosilicate one-compartment glass cell using a conventional three-electrode setup (half-cell). A hydrogen electrode in the same solution immersed in a Luggin capillary and platinum foil ( $1 \text{ cm}^2$ ) were used as reference and counter electrodes, respectively. All potentials are referred to the reversible hydrogen electrode (RHE) scale. The working electrode was a glassy carbon (GC) holder of  $0.07068 \text{ cm}^2$  of internal area, polished with  $0.03 \mu\text{m}$  alumina before each experiment and used as substrate for electrocatalyst films. The catalysts were applied to the GC by transferring  $5 \mu\text{L}$  of a sonicated catalyst ink using a microsyringe and dried at room temperature. The 'ink' consisted of 3 mg catalyst powder,  $30 \mu\text{L}$  Nafion<sup>®</sup> solution (5 wt % solution, Sigma-Aldrich) and  $600 \mu\text{L}$  isopropyl alcohol. The amount of catalyst ink was regulated to a metal loading of  $2.25 \text{ mg cm}^{-2}$  for all catalysts.

Electrochemical tests were carried out in an Autolab Model PGSTAT 302 N potentiostat/galvanostat (Eco Chemie B.V, Holland). All the electrochemical experiments were conducted using a  $0.5 \text{ M}$  potassium hydroxide ( $\text{KOH}$ ,  $\geq 99.5\%$ , Sigma-Aldrich) solution and ultrapure water (Millipore-Q<sup>™</sup>) at  $25^\circ\text{C}$ . The cyclic voltammograms (CVs) were recorded between the potential limits of  $-0.05 \text{ V}$  and  $+1.2 \text{ V}$  at  $20 \text{ mV s}^{-1}$  and under continuous purging with high-purity nitrogen.

The EOR activities were analyzed by cyclic voltammetry at different potentials (1.1, 1.2, 1.4 and  $1.5 \text{ V}$  in  $0.5 \text{ M KOH} + 0.5 \text{ M ethanol}$  at  $20 \text{ mV s}^{-1}$ ) and by chronoamperometric experiments, after applying a potential step from  $-0.05$  to  $1.2 \text{ V}$ , performed at  $0.4 \text{ V}$  for 3600 s.

### 2.4. In situ FTIR measurements

The in situ FTIR experiments were performed using a Nicolet 6700 spectrometer equipped with a mercury cadmium telluride detector cooled with liquid nitrogen. The radiation passed sequentially through a  $\text{CaF}_2$  window and reached a thin layer ( $\sim 2 \mu\text{L}$ ) of the catalyst suspension placed onto a gold electrode polished with alumina powder

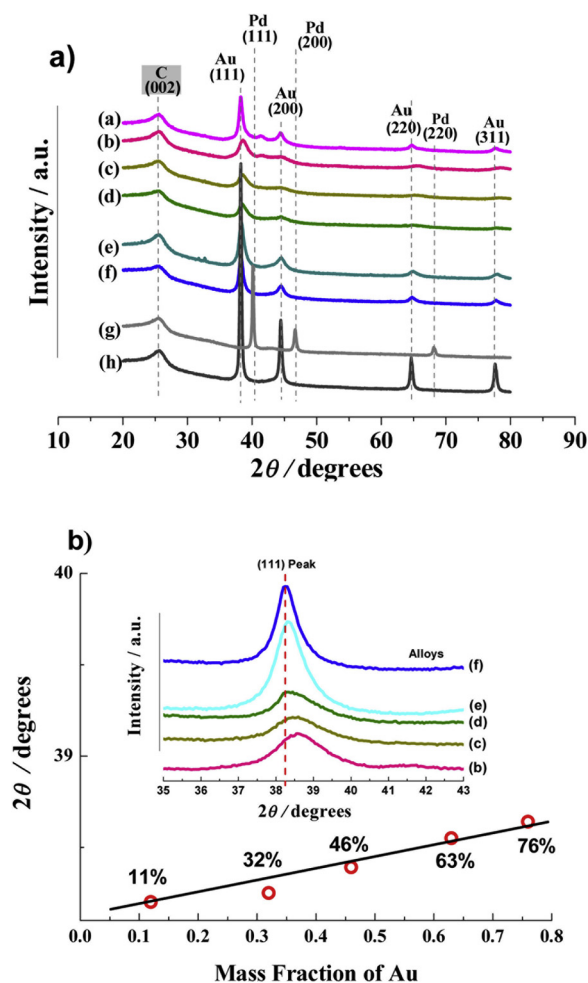


**Fig. 1.** a) X-ray diffraction patterns for the nanoparticles: (a) Au<sub>80</sub>@Pd<sub>20</sub>/C, (b) Au<sub>10</sub>Pd<sub>90</sub>/C, (c) Au<sub>30</sub>Pd<sub>70</sub>/C, (d) Au<sub>50</sub>Pd<sub>50</sub>/C, (e) Au<sub>70</sub>Pd<sub>30</sub>/C, (f) Au<sub>80</sub>Pd<sub>20</sub>/C compared with (g) Pd/C and (h) Au/C. b) Positions of the (111) Au reflections versus the mass fractions of Au. The inset shows the (111) Au reflections.

(0.05 μm) and reflected on the electrode surface. Spectra were computed from the average of 50 interferograms and the spectral resolution was set to 4 cm<sup>-1</sup>. The reflectance spectra were recorded under the same conditions after successive jumps of 0.1 V from E = 0.1 to 1.2 V and compared to a reference spectrum taken at E<sub>ref</sub> = 0.05 V. The equilibrium at each potential was reached within 5 s before each sample

**Table 1**

Molar ratio between catalysts, particles sizes obtained by TEM, average crystallite sizes, microstrain and lattice parameter estimated by XRD data.

Electrocatalyst		Particle size <sup>b</sup> (nm)	Crystallite size <sup>c</sup> (nm)	Microstrain <sup>c</sup> (%)	Lattice parameter (Å)	
Nominal	Experimental					
Atomic fraction	Mass fraction <sup>a</sup>					Atomic fraction <sup>a</sup>
Pd/C	Pd/C	Pd/C	—	18(2)	0.03	3.8918(6)
Au/C	Au/C	Au/C	—	20(2)	0.01	4.0768(2)
Au <sub>10</sub> Pd <sub>90</sub> /C	Au <sub>11</sub> Pd <sub>89</sub> /C	Au <sub>06</sub> Pd <sub>94</sub> /C	4.71	4.8(9)	0.08	4.075(3)
Au <sub>30</sub> Pd <sub>70</sub> /C	Au <sub>32</sub> Pd <sub>68</sub> /C	Au <sub>20</sub> Pd <sub>80</sub> /C	4.82	5.1(9)	0.09	4.066(2)
Au <sub>50</sub> Pd <sub>50</sub> /C	Au <sub>46</sub> Pd <sub>54</sub> /C	Au <sub>32</sub> Pd <sub>68</sub> /C	5.21	2.0(5)	0.28	4.058(4)
Au <sub>70</sub> Pd <sub>30</sub> /C	Au <sub>63</sub> Pd <sub>37</sub> /C	Au <sub>75</sub> Pd <sub>25</sub> /C	5.72	2.1(5)	0.30	4.050(9)
Au <sub>80</sub> Pd <sub>20</sub> /C	Au <sub>76</sub> Pd <sub>24</sub> /C	Au <sub>72</sub> Pd <sub>28</sub> /C	6.12	4.8(8)	0.18	4.049(2)
Au <sub>80</sub> @Pd <sub>20</sub> /C	Au <sub>85</sub> @Pd <sub>15</sub> /C	Au <sub>83</sub> @Pd <sub>17</sub> /C	5.95	5.1(8)	0.05	4.074(1)

Uncertainty inside parenthesis are for the last algorithm. Ex. 3.8918(6) means 3.8918 ± 0.0006.

<sup>a</sup> Experimental data (%) obtained by EDX.

<sup>b</sup> Particle size determined from TEM data.

<sup>c</sup> Crystallite size estimated from XRD data using Williamson-Hall plot.

spectrum collection.

### 3. Results and discussion

#### 3.1. Physical characterization

Fig. 1 shows the XRD patterns of the PdAu bimetallic catalysts supported on carbon and the corresponding monometallic nanoparticles. All XRD patterns show a broad peak at about 25.6°, which is related to the graphite-like crystalline structure of the carbon support (according to JCPDS No.00-003-0401). In Fig. 1a the Pd/C electrocatalyst shows three diffraction peaks (ca. 2θ = 40.2, 46.7 and 68.1°, JCPDS No. 00-046-1043) that are associated to the Pd (111), (200), and (220) planes [26]. For the Au/C sample, four diffraction peaks are assigned to the Au (111), (200), (220) and (311) planes [41], located at ca. 2θ = 38.3, 44.4, 64.7 and 77.6° (JCPDS No.00-004-0784), respectively.

The crystalline features of the Au are clearly present in Au@Pd/C and their values of 2θ at about 38.3, 44.4, 64.7 and 77.7° are the same taken for Au/C nanoparticles. This is due to the dominant amount of Au in the core-shell nanoparticle [42]. As previously observed for Au@Pd nanoparticles [35], this is because the Pd shell formed over the Au core is very thin, as can be seen in the TEM results (Fig. 4e) and discussed hereafter.

The full width at half maximum (β) of the Bragg peaks for Au phase was used to estimate the average crystallite size and microstrain according Williamson-Hall plot obeying Eq. (1)

$$\beta = \frac{0.89\lambda}{d_m \cos \theta} + 4\epsilon \tan \theta \quad (1)$$

where λ is wavelength, d<sub>m</sub> is average crystallite size and ε is the microstrain [54,55]. The values of average particle sizes and lattice parameters are summarized in Table 1.

Note that in Fig. 1a the main peak of the Pd (111) for the Au<sub>80</sub>@Pd<sub>20</sub>/C catalyst is slightly shifted to higher values of 2θ. Such behavior of Au@Pd/C core-shell catalysts has been reported previously in the literature [47–50] and can be attributed to a modification of the Pd lattice by lattice mismatch between the Au core and Pd shell, as is seen in Table 1. Moreover, some degree of interdiffusion can take place at the interface.

Moreover, each diffraction peak of the Au<sub>1-x</sub>Pd<sub>x</sub>/C alloys was located between those of Au/C and Pd/C catalyst [29]. Interestingly, the Au (111) peak shifts to high angle with increasing Pd/Au ratio (inset in Fig. 1b). This is because Pd atoms occupy the Au crystal lattice, resulting in a decrease in the lattice parameter (a) [51,52] (Table 1). These results are in accordance with results presented by Al-Odail et al.

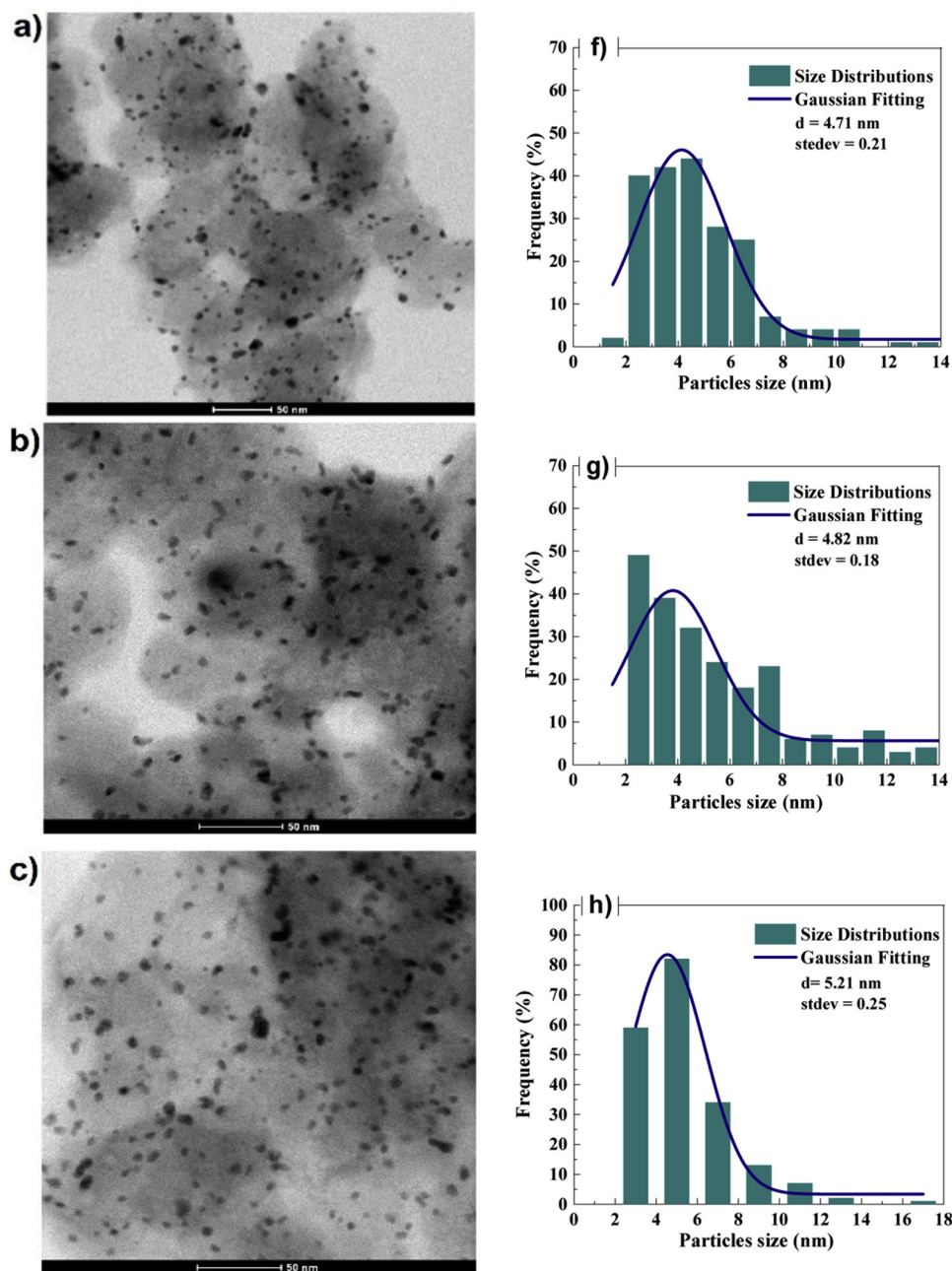


**Fig. 2.** a–e) TEM images and f–j) histograms of the average particles size distribution for  $\text{Au}_{1-x}\text{Pd}_x/\text{C}$  alloys:  $\text{Au}_{10}\text{Pd}_{90}/\text{C}$ ,  $\text{Au}_{30}\text{Pd}_{70}/\text{C}$ ,  $\text{Au}_{50}\text{Pd}_{50}/\text{C}$ ,  $\text{Au}_{70}\text{Pd}_{30}/\text{C}$  and  $\text{Au}_{80}\text{Pd}_{20}/\text{C}$ , respectively.

[53] and Simões et al. [27] for PdAu alloy nanoparticles, thus indicating the formation of  $\text{Au}_{1-x}\text{Pd}_x/\text{C}$  alloy nanoparticles. A good linear correlation ( $R^2 = 0.9582$ ) was found between the positions of the diffraction peaks and the mass fractions of Au obtained by EDX data (Table 1), as shown in Fig. 1b.

The broadening of the diffraction peaks for the  $\text{Au}_{1-x}\text{Pd}_x/\text{C}$  alloys in Fig. 1a can be attributed to the increase in residual strain due to the mismatch of the Au and Pd atomic sizes [56], as is displayed in Table 1.

Fig. 2 shows the TEM images and histograms of particle size distribution of the  $\text{Au}_{1-x}\text{Pd}_x/\text{C}$  samples. From Fig. 2(a–e), well-dispersed  $\text{Au}_{1-x}\text{Pd}_x$  nanoparticles on the carbon support are observed. It is interesting to note that Pd nanoparticles on carbon typically appear spherical, and of sizes about 4–6 nm, as observed in the histograms in Fig. 2f–j.

The average particles size ( $d_m$ ) obtained for  $\text{Au}_{1-x}\text{Pd}_x/\text{C}$  alloys catalysts are found in the same range for the catalysts  $\text{Pd}_{30}\text{Au}_{70}$  and

$\text{Pd}_{50}\text{Au}_{50}$  (5.0 and 5.1 nm, respectively) as those reported by Simões et al. [27], who synthesized Pd, Pt, Au and bimetallic PdAu and PdNi nano-catalysts supported on carbon with different compositions.

According to Table 1, the values of  $d_m$  for these nanoparticles increased from 4.71 to 6.12 nm depending on the amount of Au in the catalyst (from 11 to 76 wt %, respectively). In addition, the  $\text{Au}_{70}\text{Pd}_{30}/\text{C}$  and  $\text{Au}_{80}\text{Pd}_{20}/\text{C}$  catalysts presented agglomerated nanoparticles, which were not considered for the statistical size distribution. Geraldès et al. [57] also identified isolated agglomerates on the support with the increase in atomic percentage of Au.

The EDX analysis (Fig. 3) confirmed that the as-prepared alloy nanoparticles are composed of Au and Pd components, as expected. The nominal and EDX compositions are shown in Table 1.

Bimetallic core-shell Au–Pd nanoparticles were prepared using a seed-mediated growth strategy, which involves the synthesis of Au seed particles and the subsequent growth of a thin Pd layer. Fig. 4 shows the



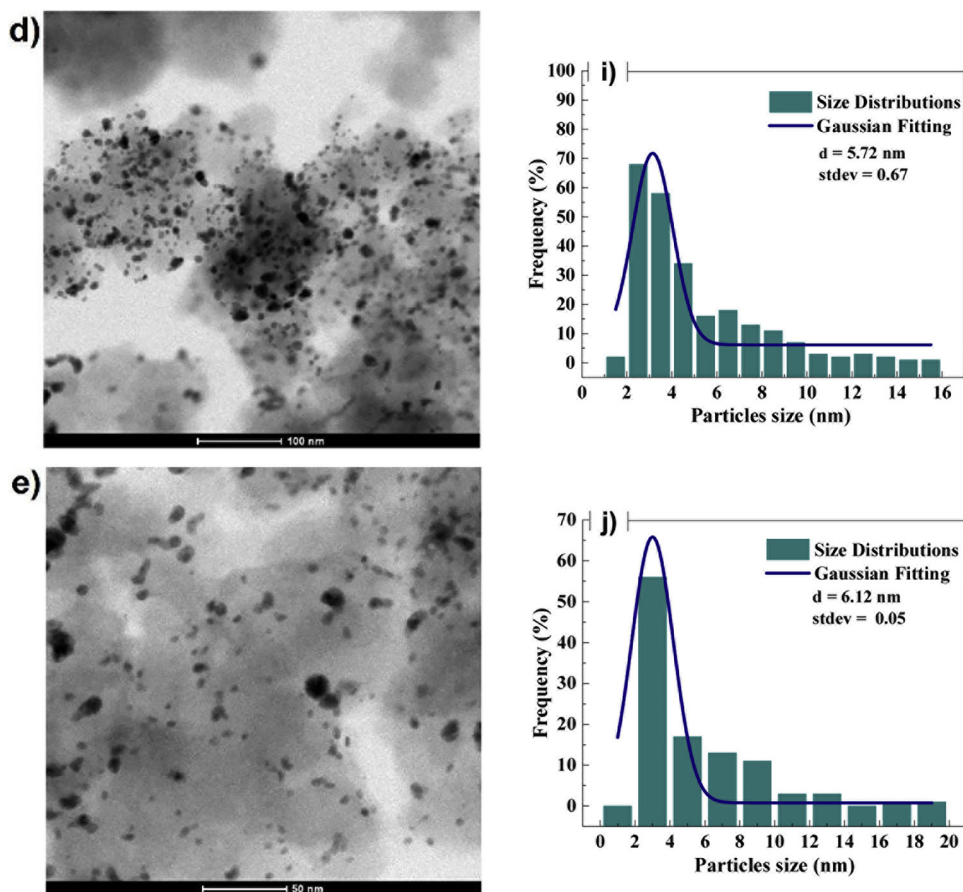


Fig. 2. (continued)

TEM, histograms of size distributions and STEM-EDX analysis, using BF and HAADF detectors of the as-prepared Au-Pd core-shell nanoparticles. Fig. 4a indicates that the core-shell particles are spherical with average particle diameter of  $5.9 \pm 0.17$  nm, despite much larger nanoparticles also being observed (Fig. 4b–g).

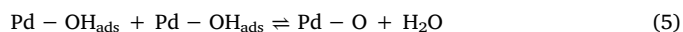
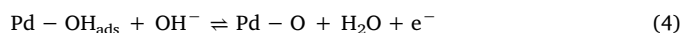
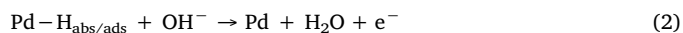
The STEM-EDX analysis (Fig. 4c) of an arbitrary single nanoparticle (shown in Fig. 4d–f) illustrates that the particles are indeed composed of Au and Pd. The formation of core-shell nanoparticles is first suggested in Fig. 4d by contrast between the core and shell regions in HAADF detector. The formation of core-shell nanoparticles with an Au core and an Ag/Pd alloy shell is again confirmed by EDX line scan (Fig. 4h) of the particle as indicated in Fig. 4e. Fig. 4g provides a scheme of the Au@Pd core-shell nanoparticle. As evidenced by Fig. 4h, Pd is detected as a predominant element on the border of the particle. Moving the electron beam inward, Au starts to be detected, while the Pd signal decreases in agreement with the increase of core to shell ratio crossed by the electron beam. A short transition layer (AuPd alloying region formed by interdiffusion between these elements) cannot be disregarded despite STEM images (BF, ADF, HAADF) suggesting a sharp interface.

### 3.2. Electrochemical characterization

The electrochemical characteristics of the Pd/C and  $\text{Au}_x\text{Pd}_{1-x}/\text{C}$  alloys, and the Au@Pd/C core-shell nanoparticles were examined to identify reactions that occur on the electrode surface. The CV curves shown in Fig. 5 were normalized to the Pd mass in each sample (obtained by EDX). Fig. 5 shows voltammograms recorded at  $20 \text{ mV s}^{-1}$  in a  $\text{N}_2$ -saturated 0.5 M KOH electrolyte in the absence and presence of ethanol.

As the catalytic reaction takes place at the electrode surface, it is

important to evaluate the surface composition of the nanoparticles. The voltammograms were swept to potentials of 1.1, 1.2, 1.4 and 1.5 V. Clearly, in Fig. 5a, the Pd/C catalyst displays well-defined hydrogen desorption/adsorption peaks and oxidation/reduction signals. In the positive scan, hydrogen desorption emerges in the potential window from  $-0.05$  to  $0.45$  V (Eq. 2), and the hydroxyl species ( $\text{OH}_{\text{ads}}$ ) adsorption appears beyond  $0.75$  V. It is widely accepted that  $\text{OH}^-$  species are first chemisorbed in the first stage of oxide formation, and then, at higher potentials, they are transformed into higher valence oxides, as described by Eqs.(3–5):



In the negative sweep, the  $\text{OH}_{\text{ads}}$  species are reduced from  $0.4$  to  $0.8$  V Eq. (6), and hydrogen formation is below  $0.1$  V. Evidently, the adsorption and desorption peaks of the hydroxyl species increase positively with the increase in electrode potential from  $1.1$  to  $1.5$  V.



For Pd content of 70 and 90%, Fig. 5c and f, respectively, hydrogen desorption/adsorption peaks are more apparent compared to the low intensities for the compositions of 30 and 20%, Fig. 5i and l, respectively. This is due to Au-based catalysts presenting weak  $\text{H}_2$  adsorption [58] in contrast to the Pd-based catalysts which present stronger  $\text{H}_2$  adsorption [30]. However, the intensity of hydrogen desorption/adsorption peaks for  $\text{Pd}_{50}\text{Au}_{50}$  (Fig. 5h) was higher than those of the alloys with higher Pd content. The differences in the surface free energy

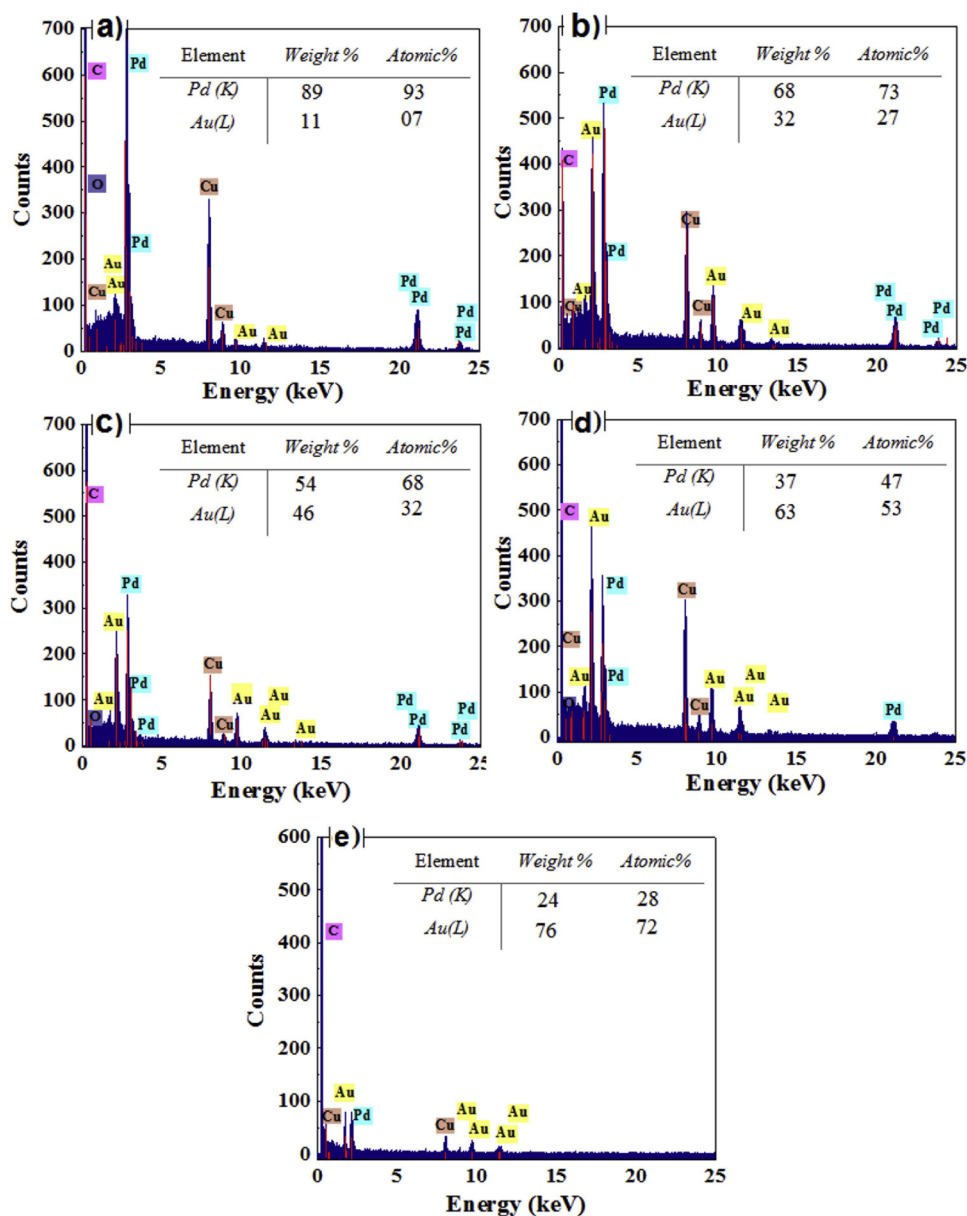


Fig. 3. EDX analysis for Au<sub>1-x</sub>Pd<sub>x</sub>/C alloys: a) Au<sub>10</sub>Pd<sub>90</sub>/C, b) Au<sub>30</sub>Pd<sub>70</sub>/C, c) Au<sub>50</sub>Pd<sub>50</sub>/C, d) Au<sub>70</sub>Pd<sub>30</sub>/C and e) Au<sub>80</sub>Pd<sub>20</sub>/C, respectively.

of Au and Pd could be responsible for the differences between  $H_{ads/des}$  on Pd<sub>50</sub>Au<sub>50</sub> and alloys with Pd contents of 70 and 90%. [59].

The surface free energy of Pd ( $2.043 \text{ J m}^{-2}$ ) is higher than that of Au ( $1.626 \text{ J m}^{-2}$ ) [60], the Au atoms preferentially segregate to the surface of the nanoparticle to minimize the surface free energy. Xu et al. [43] reported that for the PdAu alloys with low content of Au, the degree of Au segregation to the surface was higher than those with high content of Au. The same trend was observed by Liu et al. [59]. Thus, the proportion of the randomly exposed Pd atoms at the Au<sub>10</sub>Pd<sub>90</sub>/C and Au<sub>30</sub>Pd<sub>70</sub>/C catalysts surfaces can be smaller than at Au<sub>50</sub>Pd<sub>50</sub>/C, which would lead to the decrease in the intensity of hydrogen desorption/adsorption peaks. Moreover, for the catalysts with Au content > 50% (Au<sub>70</sub>Pd<sub>30</sub>/C and Au<sub>80</sub>Pd<sub>20</sub>/C alloys), the excess of Au tends to block the active sites of Pd.

In addition, an Au oxide reduction peak at 1.15 V appears in the voltammograms, which means that Au catalytic sites are also present on the Au<sub>1-x</sub>Pd<sub>x</sub>/C surface [61–65]. Similar results were found by Simões et al. [27]. Rand and Woods [61] reported that a second cathodic peak develops with continued electrode cycling, becoming close to that for

Au. It was proposed that the change in electrosorption properties is associated with preferential dissolution of palladium from the electrode surface. This greater exposure of gold atoms is observed for the Au<sub>50</sub>Pd<sub>50</sub>/C, Au<sub>70</sub>Pd<sub>30</sub>/C and Au<sub>80</sub>Pd<sub>20</sub>/C alloys, Figs. 5g, i and l, respectively.

For alloys, the increase in the amount of oxide with the increase in electrode potential is well-defined. The irreversibility of the process for high anodic potentials of the Au<sub>10</sub>Pd<sub>90</sub>/C, Au<sub>30</sub>Pd<sub>70</sub>/C and Au<sub>50</sub>Pd<sub>50</sub>/C catalysts reflect in the negative shift of surface oxide reduction peaks, characteristic of materials containing palladium [66,67].

The successive shift of the oxide reduction potential peak is also observed for Au@Pd/C catalysts. As shown in Fig. 5n, the Au@Pd/C core-shell clearly presents a homogenous distribution of Pd on the nanoparticle shell, as previously indicated by HAADF, DF and BF images, Fig. 4d–f and h, respectively. It is interesting to highlight that no noticeable Au oxide formation or reduction region was observed in the voltammograms when compared to the alloys. This fact indicates that the catalyst surface is mainly composed of Pd catalytic sites.

The EOR measurements were performed in N<sub>2</sub>-saturated 0.5 M

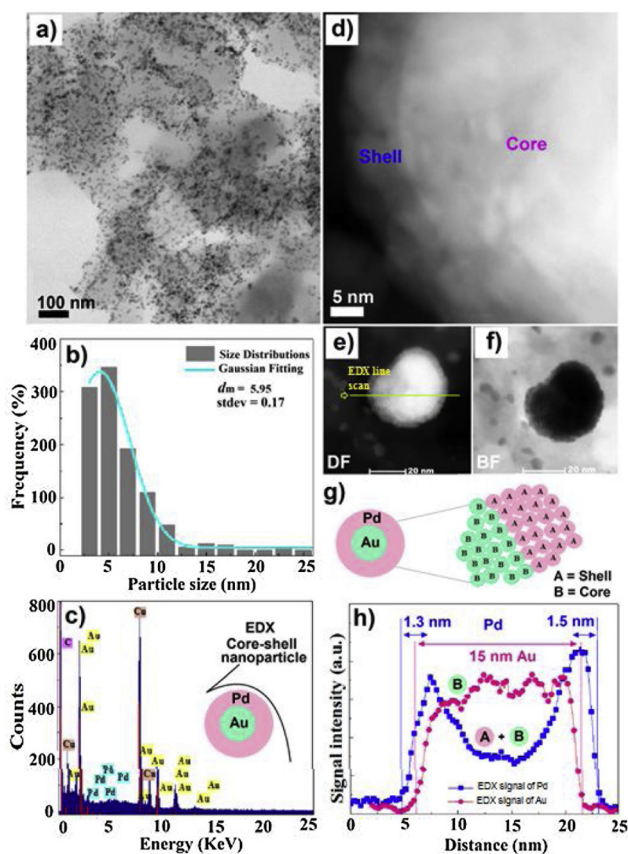


**Fig. 4.** a) TEM images of the Au@Pd/C nanoparticle and b) size distribution histogram; EDX spectra of Fig. 4a, c) STEM-EDX analyses, d) 5 nm magnification HRTEM image, e) HAADF-STEM image, f) bright-field TEM image, g) scheme of the core-shell Au@Pd/C structure, h) EDX line scan signal of an Au@Pd core-shell nanoparticle. The values indicate a mean core diameter of 15 nm and a shell thickness of 2.8 nm.

KOH + 0.5 M ethanol. Fig. 5 shows the ethanol electro-oxidation mass activities of the all samples by CVs at different potentials. The CVs of ethanol electro-oxidation with all the catalysts consist of two parts; namely, the forward scan and the reverse scan [65]. The hydrogen desorption/sorption region, below 0.4 V, is clearly suppressed in the presence of ethanol in the solution. The EOR proceeds continuously such that the current continues to increase with the potential, indicating that the covered active surface sites are refreshed with the assistance of adsorbed OH species [67].

The potential peak ( $E_{\text{peak}}$ ) of ca. 0.80 V for Pd/C, Au<sub>10</sub>Pd<sub>90</sub>/C and Au@Pd/C and  $E_{\text{peak}} > 0.80$  V for the other alloys appear in the forward scan. The EOR reaches the maximum value and then starts to decline with a further increase in the potential. This decrease is due mainly to the formation of an oxide layer on the surface of the electrode at higher potentials (Eqs. 4 and 5). The peak in the reverse scan results from the removal of the incompletely oxidized carbonaceous species (e.g., CH<sub>3</sub>CO<sub>ads</sub> or CO<sub>ads</sub>) formed in the forward scan [67], as well as from the alcohol oxidation on the clean catalyst surface after oxide reduction in the backward scan.

Evidently, with the addition of Au to the Pd in the catalysts, i.e., Au<sub>10</sub>Pd<sub>90</sub>/C, Au<sub>30</sub>Pd<sub>70</sub>/C and Au<sub>50</sub>Pd<sub>50</sub>/C, Fig. 5d, f, h respectively, the bimetallic nanoparticles promote a beneficial effect on the performance in the whole applied potential range. Increases of 8, 21 and 29% in mass activity measured at the upper limit of 1.1 V for Au<sub>10</sub>Pd<sub>90</sub>/C, Au<sub>30</sub>Pd<sub>70</sub>/C and Au<sub>50</sub>Pd<sub>50</sub>/C, respectively, compared with the monometallic Pd/C catalyst, Fig. 5b, were observed.

However, the Au<sub>70</sub>Pd<sub>30</sub>/C and Au<sub>80</sub>Pd<sub>20</sub>/C catalysts had lower catalytic activity compared to the Pd/C catalyst. This can be due to a low

concentration of Pd atoms on the surface of the catalysts [68]. Another possibility may be related to the negligible effect of the carbon-supported pure gold for EOR [69,70].

The best performance of the electrocatalyst-forming alloys may be attributed to the bifunctional mechanism, where a greater number of Pd atoms are available for ethanol adsorption, and Au provides oxygen species for the oxidation of the intermediates [71]. Beden et al. [72] showed that, in alkaline medium, oxygenated species could adsorb on the gold surface from potentials as low as 0.4 V, which may explain the onset potential ( $E_{\text{onset}}$ ) of ca. 0.4 V found in our work.

The mass activity at the current maximum value of the forward scan (upper limit of potential of 1.1 V) of the Au@Pd/C catalyst is almost twice that of the Pd/C (826.2 mA mg<sup>-1</sup>, Fig. 5o, and 453.4 mA mg<sup>-1</sup> Pd, respectively). The mass increase (45%) for the Au@Pd/C catalyst, by formation of an overlaying Au<sub>core</sub> ← Pd<sub>shell</sub> bimetallic nanostructure should be emphasized. This behavior might be ascribed to a downshift in the Pd *d*-band center. Thus, during ethanol electro-oxidation the adsorption of carbonaceous intermediates on the Pd sites is much weakened, and a further increase in the hydrogen binding strength is seen [73]. High hydrogen adsorption currents observed for Au@Pd/C in Fig. 5n confirm this assumption. On the other hand, the increase in the mass activity is mainly due to the synergistic effect between Au and Pd (such as ensemble effect [74], geometric effect [36], and electronic effect [73]) [36].

This significant enhancement can be related to the core-shell structure, particularly the interaction between the Au core and the thin Pd shell (2.8 nm). Roudgar and Groß [75] tested the local reactivity of thin pseudomorphic Pd overlayers on Au (111) and (100) single-crystal surfaces. According to them, the highest reactivity was obtained for the thinnest Pd layers in the particles studied, which had a height corresponding to two to three layers. They concluded that the high electrochemical reactivity is a consequence of the combination of substrate interaction and lattice mismatch effects.

Moreover, the change of the upper limit of potential (from 1.1 V to 1.5 V) is not beneficial for EOR for all catalysts. This is related to loss of electrode material due to electrochemical dissolution of Pd [49]. The calculated loss of mass activity when extending the potential limit window from 1.1 to 1.5 V was 46% (Pd/C), 45% (Au<sub>10</sub>Pd<sub>90</sub>/C), 42% (Au<sub>30</sub>Pd<sub>70</sub>/C), 37% (Au<sub>50</sub>Pd<sub>50</sub>/C), 45% (Au<sub>70</sub>Pd<sub>30</sub>/C), 51% (Au<sub>80</sub>Pd<sub>20</sub>/C) and 19% (Au@Pd/C), indicating that the Au core could improve the resistance to dissolution at high anodic potentials in alkaline solution.

Koh et al. [76] synthesized Ag@Pt core-shell catalysts supported on carbon. The Ag@Pt catalysts were more stable than monolithic Pt catalysts. This is because the Pt shell in Ag@Pt catalysts exhibits lower Pt chemical potential than in Pt catalysts, thus reducing the tendency for dissolution and Ostwald ripening. Lower chemical potential of Pt in the shell is attributed to the larger lattice parameter of Ag compared to Pt. The same behavior may be extended to the Au@Pd catalyst. The specific mass activities of Pd/C, Au<sub>1-x</sub>Pd<sub>x</sub>/C alloys and Au@Pd/C core-shell structure calculated from the forward scan currents on all upper limit potentials (1.1, 1.2, 1.4 and 1.5 V) are listed in Table 2.

The electrocatalytic stability of the as-prepared catalysts for ethanol oxidation was studied by chronoamperometry in 0.5 M KOH + 0.5 M ethanol solution at 0.4 V, as shown in Fig. 6. The long-term stability (%  $\delta$ ) is evaluated by measuring the linear current decay using Eq. (7), as described in earlier reports [77,78]:

$$\delta (\%s^{-1}) = \frac{100}{i_0} \times \left( \frac{d_i}{d_t} \right)_{t > 500s} \quad (7)$$

where  $(d_i/d_t)_{t > 500s}$  (on a normalized scale) is the current decay linear portion slope, and  $i_0$  is the current at the onset of polarization back-extrapolated from the linear current decay. From the typical current density-time responses of Fig. 6a, an initial drop is observed on all current-time curves due to the accumulation of the strongly adsorbed reactive intermediates (CH<sub>3</sub>CO<sub>ads</sub>) and the ultimate poisoning species



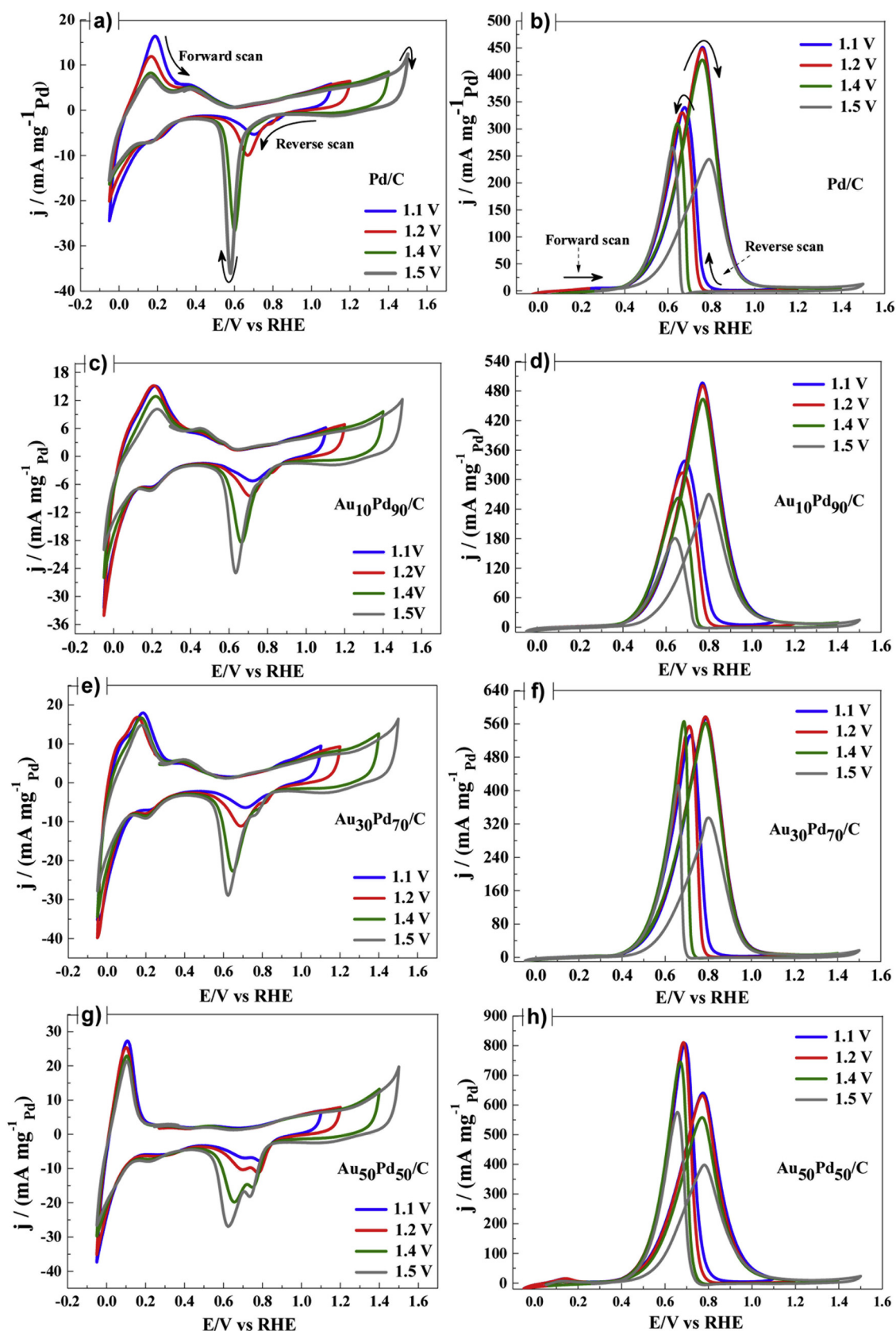


Fig. 5. Cyclic voltammograms at scan rate  $20 \text{ mV s}^{-1}$  in 0.5 M KOH, and in 0.5 M KOH solution containing 0.5 M ethanol: a, b) Pd/C; c, d)  $\text{Au}_{10}\text{Pd}_{90}/\text{C}$ ; e, f)  $\text{Au}_{30}\text{Pd}_{70}/\text{C}$ ; g, h)  $\text{Au}_{50}\text{Pd}_{50}/\text{C}$ ; i, j)  $\text{Au}_{70}\text{Pd}_{30}/\text{C}$ ; l, m)  $\text{Au}_{80}\text{Pd}_{20}/\text{C}$  and n, o)  $\text{Au}_{80}@ \text{Pd}_{20}/\text{C}$  catalysts, respectively. Current density normalized to the Pd mass.



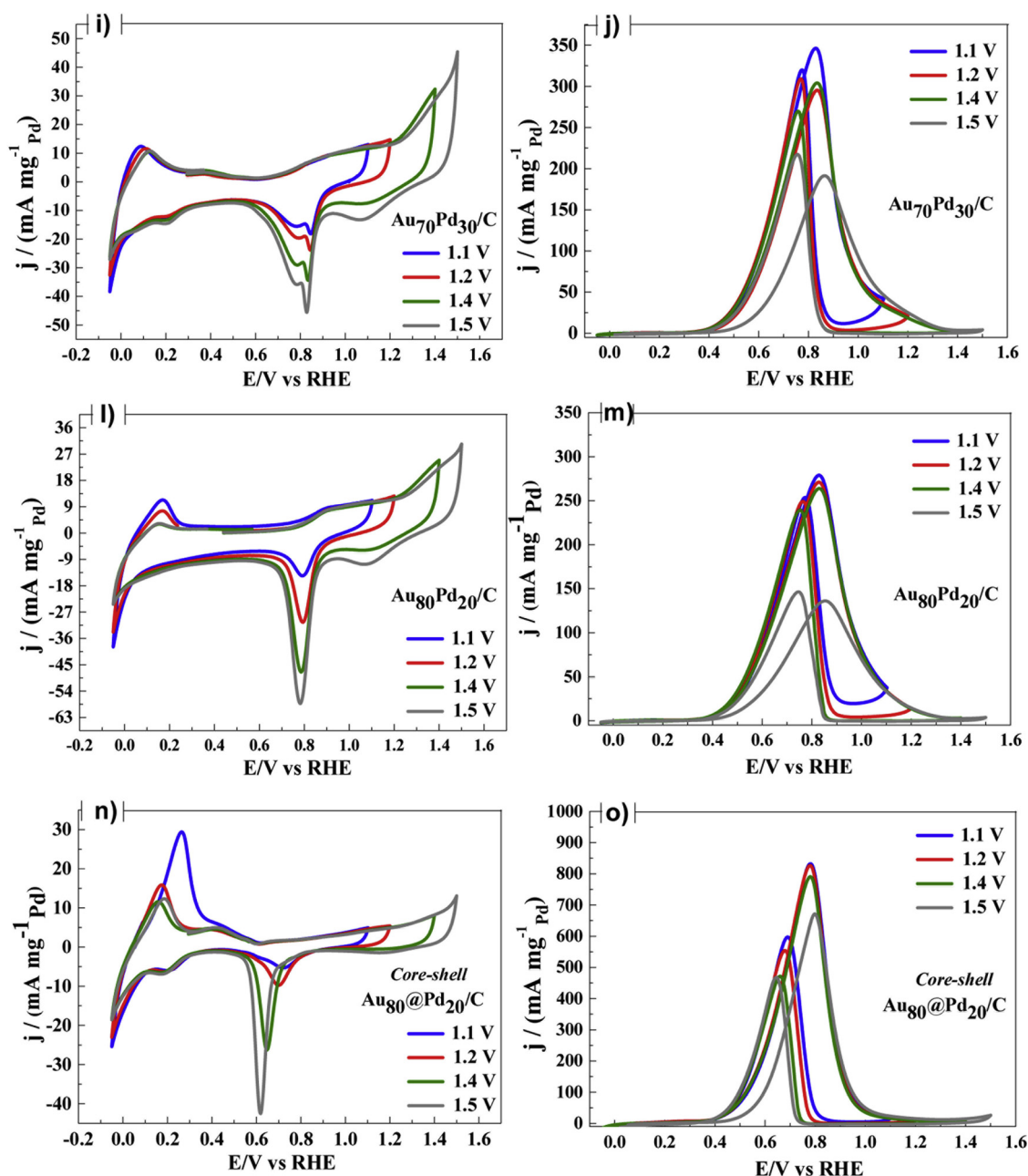


Fig. 5. (continued)

Table 2

Values of mass activity (MA) of the Pd/C, Au<sub>x</sub>Pd<sub>1-x</sub>/C alloys and core-shell Au@Pd/C nanoparticles.

Electrocatalyst	Mass activity/mA mg <sup>-1</sup>			
	E/1.1 V	E/1.2 V	E/1.4 V	E/1.5 V
Pd/C	453.4	453.4	426.8	242.7
Au <sub>10</sub> Pd <sub>90</sub> /C	497.1	488.8	461.9	271.7
Au <sub>30</sub> Pd <sub>70</sub> /C	574.4	574.4	562.2	332.5
Au <sub>50</sub> Pd <sub>50</sub> /C	640.1	629.7	557.1	398.1
Au <sub>70</sub> Pd <sub>30</sub> /C	346.7	303.8	295.3	189.6
Au <sub>80</sub> Pd <sub>20</sub> /C	279.2	271.4	263.2	136.5
Au <sub>80</sub> @Pd <sub>20</sub> /C	826.2	826.2	788.2	666.7

(CO<sub>ads</sub>) of ethanol oxidation on the active surface sites of the catalysts.

Nevertheless, the Au@Pd/C core-shell catalyst presented the higher current density after 3600 s, followed by Au<sub>10</sub>Pd<sub>90</sub>/C, Au<sub>30</sub>Pd<sub>70</sub>/C,

Au<sub>50</sub>Pd<sub>50</sub>/C alloys, as compared to Pd/C. This agrees with the results of the cyclic voltammetry experiments for ethanol oxidation (Fig. 5). The bearing of high oxidation current by the Au@Pd/C catalyst is due to the Au core effect of weakening the adsorption strength of CO-like species on the Pd shell. Fig. 6b shows the mass activity and specific activity of the catalysts for the current after 3600 s of experiment. The specific activity of the catalysts was evaluated by considering the charges required for the reduction of PdO monolayer were taken to be 405 μC cm<sup>-2</sup>, as already reported [31].

The poisoning rate (% δ) decreases in the order: 2.16 > 2.11 > 1.95 > 1.91 > 1.09 > 0.70 > 0.14% s<sup>-1</sup> for Au<sub>20</sub>Pd<sub>80</sub>/C, Au<sub>70</sub>Pd<sub>30</sub>/C, Au<sub>30</sub>Pd<sub>70</sub>/C, Pd/C, Au<sub>10</sub>Pd<sub>90</sub>/C, Au<sub>50</sub>Pd<sub>50</sub>/C and Au@Pd/C catalysts, respectively. The lower poisoning rate of the core-shell compared to all the catalysts studied indicates that it possesses a higher tolerance to intermediate species formed during the EOR.

Fig. 7 displays in situ FTIR reflectance spectra of ethanol oxidation

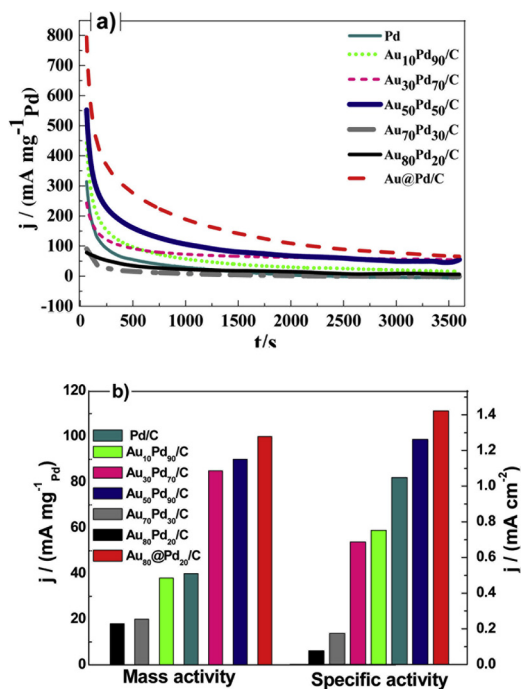
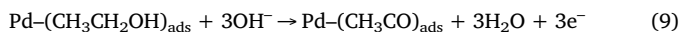
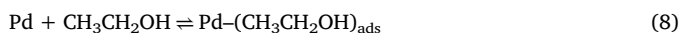


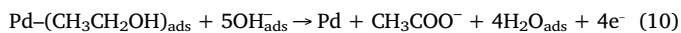
Fig. 6. a) Chronoamperometric curves in 0.5 M ethanol + 0.5 M KOH solution for 3600 s at 0.4 V versus RHE potential and b) Mass activities and specific activities of current after 3600 s of experiment for Pd/C, Au@Pd/C and Au<sub>1-x</sub>Pd<sub>x</sub>/C catalysts.

at potentials varying from 0.6 to 1.2 V at intervals of 0.1 V in 0.5 M KOH + 0.5 M ethanol on the Au<sub>1-x</sub>Pd<sub>x</sub>/C, Au<sub>80</sub>@Pd<sub>20</sub>/C, Au/C and Pd/C electrocatalysts in order to analyze the formation of intermediates and reaction products.

Down-pointing (negative) bands denote the production of species in the thin layer contained between the working electrode and the CaF<sub>2</sub> flat window, while up-pointing (positive) bands represent the consumption or depletion of other species. The positive bands located at 1047 and 1088 cm<sup>-1</sup> are assigned to C–O stretch, a characteristic absorption of ethanol, which reveals the consumption of ethanol due to the oxidation, as seen in the following reactions:



For all spectra taken at the studied electrocatalysts, two intense negative (down-pointing) bands at 1551 and 1415 cm<sup>-1</sup> were observed. Those bands can be attributed to vibrations of asymmetric and symmetric C–O bonds, characteristic of the presence of acetate ions (CH<sub>3</sub>COO<sup>-</sup>) [77–79]. A weak band at 1347 cm<sup>-1</sup> also can be attributed to acetate ions [5], as seen in the following Eq. (10):



A weak band at 2342 cm<sup>-1</sup> can be associated to symmetrical stretching vibrations of O=C=O, which corresponds to cleavage of the C–C bond in the oxidation of ethanol to CO<sub>2</sub> [80,81]. Geraldies et al. [69] observed, in Pd/C, Au/C and AuPd/C electrocatalysts, bands corresponding to the formation of CO<sub>2</sub> at a wavenumber of ~2342 cm<sup>-1</sup>, for ethanol oxidation in 0.1 mol L<sup>-1</sup> of KOH, similar to the one found in this work (~2342 cm<sup>-1</sup>).

According to Zhou et al. [5], the appearance of the CO<sub>2</sub> band also suggests that most of the OH<sup>-</sup> species of the KOH base in the thin-layer solution has been consumed due to ethanol oxidation, as described by Eqs. (10) and (11):



For Au<sub>10</sub>Pd<sub>90</sub>/C and Au<sub>80</sub>@Pd<sub>20</sub>/C electrocatalysts, the band at 2342 cm<sup>-1</sup> appears when E > 1.0 V. For the other Au<sub>1-x</sub>Pd<sub>x</sub>/C alloys, the presence of CO<sub>2</sub> was observed at E = 1.2 V. However, for Pd/C and Au/C, the presence of acetate bands only was observed, demonstrating the preference for the C2 pathway, which maintains the C–C bond intact. The higher current densities observed in the cyclic voltammetry (Fig. 5o) for Au<sub>80</sub>@Pd<sub>20</sub>/C electrocatalyst may be related to the higher CO<sub>2</sub> production.

The enhanced performance of Au<sub>80</sub>@Pd<sub>20</sub>/C core-shell catalyst for CO<sub>2</sub> formation can be ascribed to electronic effects. Modifications in the binding energies of Pd on the Au<sub>80</sub>@Pd<sub>20</sub>/C electrocatalyst could decrease the adsorption energy of CO on Pd and favor C–H cleavage on Pd sites owing to the shift of the d-band center [82]. In addition, Au could advance the oxidation of CO, eliminating the CO intermediates more easily and, as a result, increase the catalyst tolerance [82], as is possible to observe in the chronoamperometric tests of Fig. 6a.

It should be pointed out that the band located at ~1840 cm<sup>-1</sup>, attributed to the CO bonding on the surface of the electrocatalysts [83], and which is generated from the dissociative adsorption of ethanol on the electrode, was not observed for any electrocatalyst. Previously, in situ FTIR results by Fang et al. [78] reported no adsorbed species of CO to be observed either. However, in another study, Zhou et al. [5] successfully detected a weak band of CO. This divergence can be attributed to the employment of a different FTIR method that has higher detection sensibility for adsorbed species.

Fig. 8 shows the potential dependence (between 0.6 and 1.2 V) of acetate and CO<sub>2</sub> band intensity in the thin-layer solution during ethanol oxidation, in order to compare the efficiency of the studied electrocatalysts.

The intensity of the acetate band for all electrocatalysts increases rapidly when the potential is higher than 0.7 V, then almost reaches a plateau at 1.0 V (Fig. 8a). Pd/C and the other Au<sub>1-x</sub>Pd<sub>x</sub>/C alloys (Au<sub>10</sub>Pd<sub>90</sub>/C, Au<sub>30</sub>Pd<sub>70</sub>/C and Au<sub>70</sub>Pd<sub>30</sub>/C) show similar acetate generation spectra, as shown in Fig. 8b. The Au<sub>10</sub>Pd<sub>90</sub>/C and Au<sub>50</sub>Pd<sub>50</sub>/C electrocatalysts presented the highest levels of acetate generation when compared to other electrocatalysts.

The results suggest that the electro-oxidation of ethanol on these catalysts occurs predominantly without C – C bond breaking, thus reducing the amount of carbonate ions and CO<sub>2</sub> generated, although weak bands of CO<sub>2</sub> are identified. Therefore, acetate is the main product of ethanol electro-oxidation in an alkaline medium [66]. The Au<sub>80</sub>@Pd<sub>20</sub>/C and Au/C electrocatalysts show the lowest generation level of acetate when compared to the other electrocatalysts (Fig. 8b).

According to Fig. 8c, the band for CO<sub>2</sub> generation for Au<sub>10</sub>Pd<sub>90</sub>/C and Au<sub>80</sub>@Pd<sub>20</sub>/C electrocatalysts was identified at least 0.1 V lower than for the other electrocatalysts. However, the band intensity (ΔR/R) for CO<sub>2</sub> generation was 77.8% higher for the core-shell electrocatalyst compared to Au<sub>10</sub>Pd<sub>90</sub>/C (Fig. 8d).

In summary, the experiments showed that the Au<sub>80</sub>@Pd<sub>20</sub>/C electrocatalyst exhibits promising activity for EOR, and the FTIR results strengthened the evidence that the presence of a core-shell structure modified the mechanism for ethanol oxidation on Pd to a mechanism more selective for CO<sub>2</sub> formation.

#### 4. Conclusion

In summary, we successfully synthesized Au<sub>1-x</sub>Pd<sub>x</sub>/C alloys and Au@Pd/C core-shell nanoparticles. The formation of an Au@Pd core-shell structure was proved by BF and STEM/EDX measurements. XRD data confirmed the presence of metallic Pd and Au. The average diameter of the nanoparticles was 4–6 nm. Electrochemical measurements indicated that the catalytic activity toward ethanol oxidation depends on the composition and structure of the catalysts. The Au@Pd/C exhibited the highest catalytic activity for EOR in alkaline media, compared with the Pd/C and Au<sub>1-x</sub>Pd<sub>x</sub>/C alloys catalysts. The catalytic activity for Au@Pd/C was two times higher, at 1.1 V, and almost three

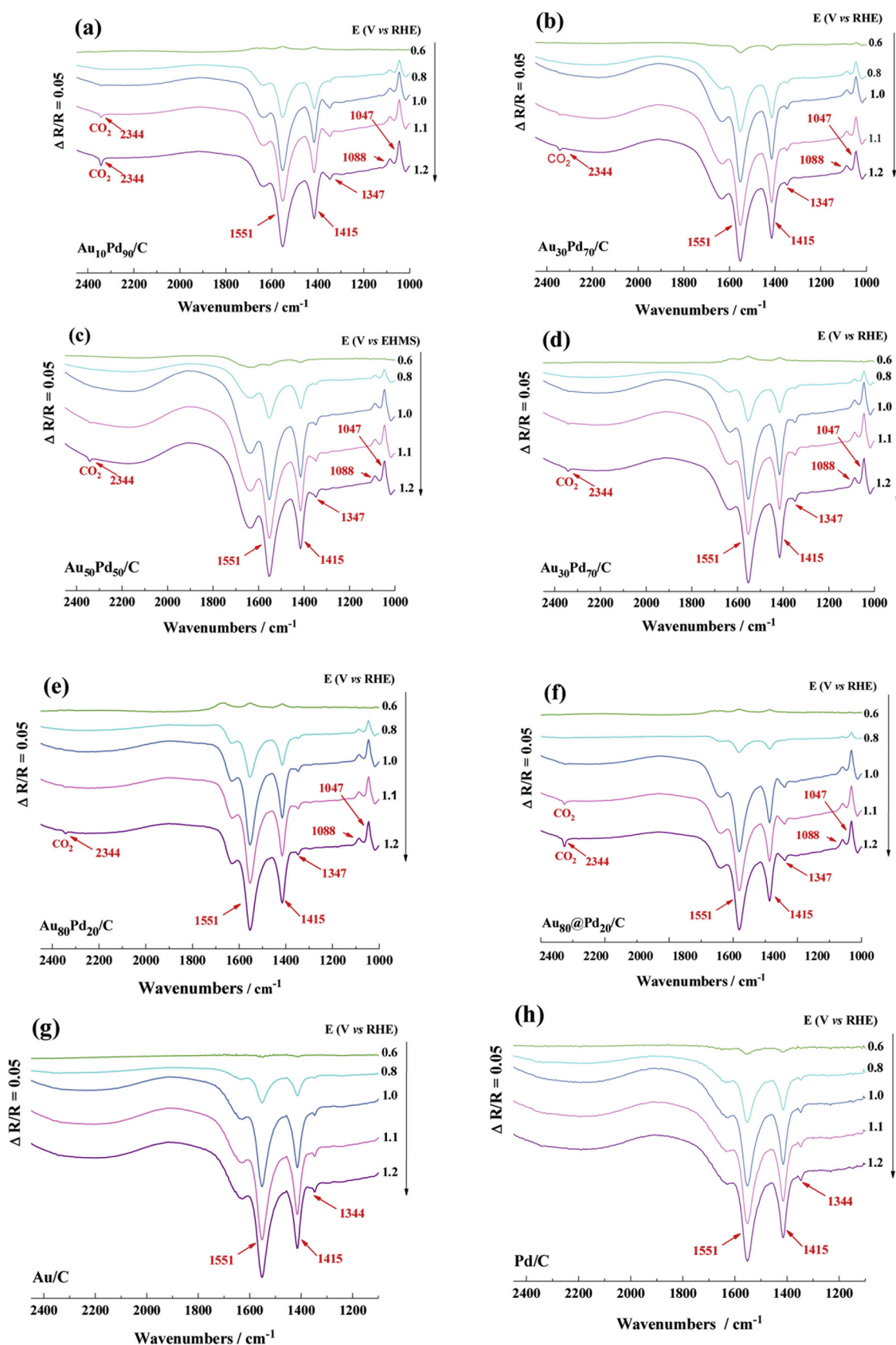
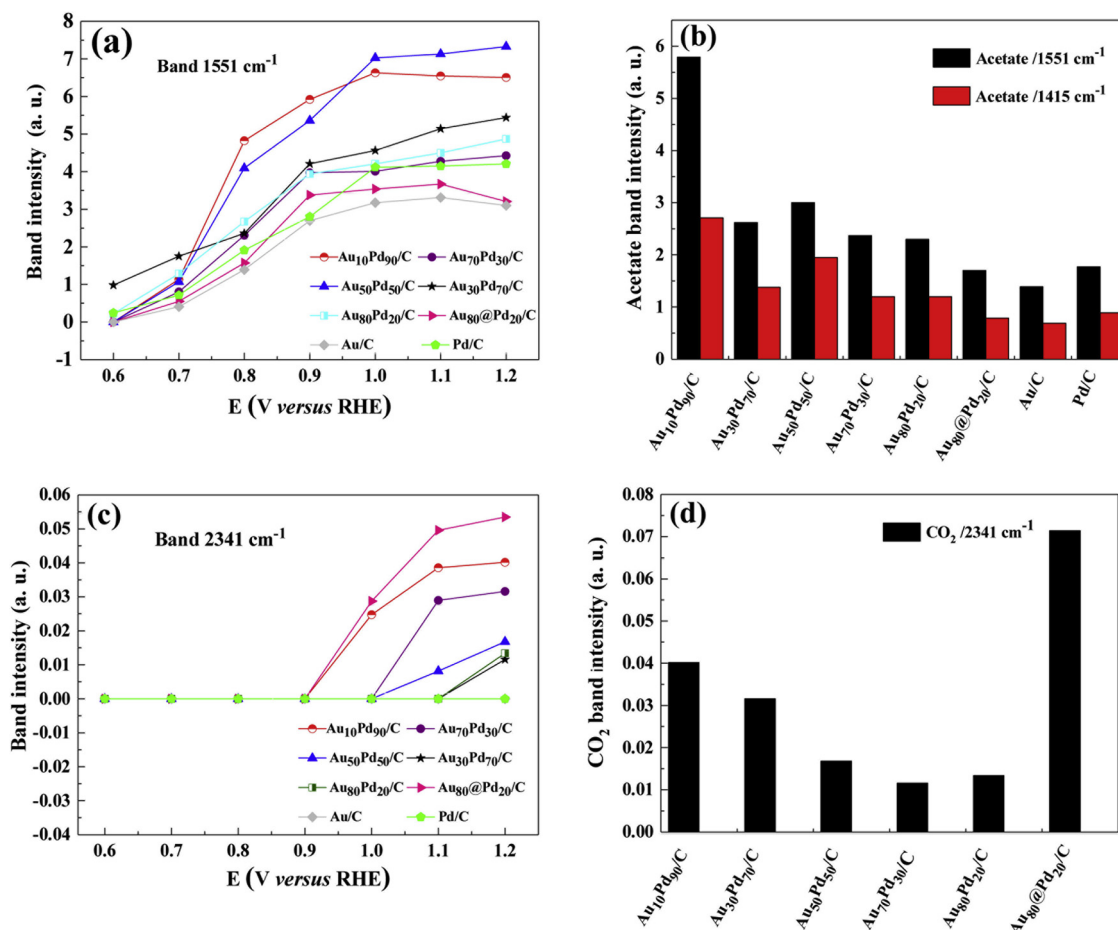


Fig. 7. In situ infrared spectra recorded in 0.5 M KOH + 0.5 M ethanol on (a)  $\text{Au}_{10}\text{Pd}_{90}/\text{C}$ , (b)  $\text{Au}_{30}\text{Pd}_{70}/\text{C}$ , (c)  $\text{Au}_{50}\text{Pd}_{50}/\text{C}$ , (d)  $\text{Au}_{70}\text{Pd}_{30}/\text{C}$ , (e)  $\text{Au}_{80}\text{Pd}_{20}/\text{C}$ , (f)  $\text{Au}_{80}@Pd_{20}/\text{C}$ , (g)  $\text{Au}/\text{C}$  and (h)  $\text{Pd}/\text{C}$  at room temperature;  $E_{\text{ref}} = 0.05$  V versus RHE. Potential range:  $E = 0.6$  and 1.2 V versus RHE. Potential step: 0.1 V.



**Fig. 8.** (a) Potential dependence of acetate band intensity generated from ethanol oxidation on Pd/C, Au/C, Au@Pd/C and Au<sub>1-x</sub>Pd<sub>x</sub>/C electrocatalysts. (b) Comparison of acetate band intensity at 1551 cm<sup>-1</sup> and 1415 cm<sup>-1</sup> for all the developed electrocatalysts at 0.8 V. (c) Potential dependence of CO<sub>2</sub> band intensity generated from ethanol oxidation on the developed electrocatalysts. (d) Comparison of CO<sub>2</sub> band intensity at 2342 cm<sup>-1</sup> for all the prepared electrocatalysts at 1.2 V.

times higher, at 1.5 V, compared to the Pd/C catalyst. AuPd alloys containing 10, 30 and 50% of Au in their composition also presented superior catalytic activity when compared to the monometallic Pd catalyst. The calculated loss of mass activity was only 19% for Au@Pd/C, against 46% for Pd/C, indicating that the core-shell structure could improve their resistance to dissolution at high anodic potentials. Chronoamperometry revealed that the addition of Au remarkably enhances the stability and electrocatalytic activity of Pd, due to the action of bifunctional effect of the Au<sub>1-x</sub>Pd<sub>x</sub>/C alloys, and the synergetic effect at Au@Pd/C. In situ FTIR experiments identified acetate as the principal product of ethanol electro-oxidation on the studied electrocatalysts. However, the Au@Pd/C core-shell structure presented the lowest levels of acetate generation and the highest levels of CO<sub>2</sub> generation, suggesting more selectivity to C – C bond breaking. Therefore, the developed approach can be used for preparing other efficient electrocatalysts for DEFCs.

#### Acknowledgment

The authors thank the Brazilian National Council of Technological and Scientific Development-CNPq (grants: 303630/2012-4, 474261/2013-1, 407274/2013-8, 402243/2012-9, 400443/2013-9 and 310282/2013-6), to Coordenação de Aperfeiçoamento de Pessoal de Nível Superior (CAPES) - finance Code 001 and to FAPITEC for the scholarships and financial support for this work.

#### References

- [1] J. Guo, R. Chen, F.-C. Zhu, S.-G. Sun, H.M. Villullas, *Appl. Catal. B* 224 (2018) 602–611.
- [2] U.K. Gupta, H. Pramanik, *Int. J. Hydrogen Energ.* 44 (2019) 421–435.
- [3] T.S. Almeida, Y. Yu, A.R. de Andrade, H.D. Abruña, *Electrochim. Acta* 295 (2018) 751–758.
- [4] L. Ning, X. Liu, M. Deng, Z. Huang, A. Zhu, Q. Zhang, Q. Liu, *Electrochim. Acta* 297 (2018) 206–214.
- [5] Z.-Y. Zhou, Q. Wang, J.-L. Lin, N. Tian, S.-G. Sun, *Electrochim. Acta* 55 (2010) 7995–7999.
- [6] X. Yang, Q. Yang, J. Xu, C.-S. Lee, *J. Mater. Chem.* 22 (2012) 8057–8062.
- [7] F.-M. Li, X.-Q. Gao, S.-N. Li, Y. Chen, J.-M. Lee, *NPG Asia Mater.* 7 (2015) e219.
- [8] P. Wu, Y. Huang, L. Kang, M. Wu, Y. Wang, *Sci. Rep.* 5 (2015) 14173.
- [9] F.J. Rodríguez Varela, O. Savadogo, *J. New Mat. Electr. Sys.* 9 (2006) 127–137.
- [10] F. Vigier, C. Coutanceau, A. Perrard, E.M. Belgsir, C. Lamy, *J. Appl. Electrochem.* 34 (2004) 439–446.
- [11] L.M. Palma, T.S. Almeida, A.R. De Andrade, *ECS Trans.* 58 (2013) 651–661.
- [12] S. Alayoglu, A.U. Nilekar, M. Mavrikakis, B. Eichhorn, *Nature Mat.* 7 (2008) 333–338.
- [13] L. Chen, H. Guo, T. Fujita, A. Hirata, W. Zhang, A. Inoue, M. Chen, *Adv. Funct. Mater.* 21 (2011) 4364–4370.
- [14] D.A. Cantane, F.H.B. Lima, *Electrocatal.* 3 (2012) 324–333.
- [15] W.J. Zhou, W.Z. Li, S.Q. Song, Z.H. Zhou, L.H. Jiang, G.Q. Sun, Q. Xin, K. Pouliantitis, S. Kontou, P. Tsiakaras, *J. Power Sources* 131 (2004) 217–223.
- [16] C. Xu, L. Cheng, P. Shen, Y. Liu, *Electrochem. Commun.* 9 (2007) 997–1001.
- [17] N. Fujiwara, Z. Siroma, S.-I. Yamazaki, T. Ioroi, H. Senoh, K. Yasuda, *J. Power Sources* 185 (2008) 621–626.
- [18] S.C.S. Lai, M.T.M. Koper, *Faraday Discuss.* 140 (2008) 399–416.
- [19] F. Colmati, G. Tremiliosi-Filho, E.R. Gonzalez, A. Berna, E. Herrero, J.M. Feliu, *Phys. Chem. Chem. Phys.* 11 (2009) 9114–9123.
- [20] H. Wang, Z. Jusys, R.J. Behm, *J. Power Sources* 154 (2006) 351–359.
- [21] E.G. Ciapina, S.F. Santos, E.R. Gonzalez, *J. Solid State Electrochem.* 17 (2013) 1831–1842.
- [22] E.G. Ciapina, S.F. Santos, E.R. Gonzalez, *J. Electroanal. Chem.* 815 (2018) 47–60.
- [23] C. Xu, L. Cheng, P. Shen, Y. Liu, *Electrochem. Commun.* 9 (2007) 997–1001.



- [24] C. Xua, P.K. Shen, Y. Liu, J. Power Sources 164 (2007) 527–531.
- [25] N. Fujiwara, Z. Siroma, S.-I. Yamazaki, T. Ioroi, H. Senoh, K. Yasuda, J. Power Sources 185 (2008) 621–626.
- [26] V. Bambagioni, C. Bianchini, A. Marchionni, J. Filippi, F. Vizza, J. Teddy, P. Serp, M. Zhiani, J. Power Sources 190 (2009) 241–251.
- [27] M. Simões, S. Baranton, C. Countanceau, J. Phys. Chem. C 113 (2009) 13369–13376.
- [28] M. Smiljanić, Z. Rakočević, S. Štrbac, Int. J. Electrochem. Sci. 8 (2013) 4941–4954.
- [29] Z. Zhang, L. Xin, K. Sun, W. Li, Int. J. Hydrogen Energ. 36 (2011) 12686–12697.
- [30] Q. He, W. Chen, S. Mukerjee, S. Chen, F. Laufek, J. Power Sources 187 (2009) 298–304.
- [31] J. Datta, A. Dutta, S. Mukherjee, J. Phys. Chem. C 115 (2011) 15324–15334.
- [32] M. Farsadrooh, J. Torrero, L. Pascual, M.A. Peña, M. Retuerto, S. Rojas, Appl. Catal. B 224 (2018) 602–611.
- [33] Q. Zhang, Z.J. Mellinger, Z. Jiang, X. Chen, B. Wang, B. Tian, Z. Liang, J.G. Chen, J. Electrochem. Soc. 165 (2018) J3031–J3038.
- [34] E.G. Ciapina, L.B. Viana, R.M.I.S. Santos, M.S.M. Nogueira, O.P. Almeida Jr, R. Nunes, S.F. Santos, R.Z. Nakazato, Int. J. Hydrogen Energy 43 (2018) 17748–17752.
- [35] W. Zhou, J.Y. Lee, Electrochem. Commun. 9 (2007) 1725–1729.
- [36] C. Hsu, C. Huang, Y. Hao, F. Liu, Nanocastle Res. Lett. 8 (2013) 113.
- [37] M. Chen, D. Kumar, C.-W. Yi, D.W. Goodman, Science 310 (2005) 291–293.
- [38] T. Ramulifho, K.I. Ozoemena, R.M. Modibedi, C.J. Jafta, Electrochim. Acta 59 (2012) 310–320.
- [39] P. Strasser, S. Koh, T. Anniyev, J. Greeley, K. More, C. Yu, Z. Liu, S. Kaya, D. Nordlund, H. Ogasawara, M.F. Toney, A. Nilsson, Nat. Chem. 2 (2010) 454–560.
- [40] C. Hsu, M. Wei, Z. Wei, F. Liu, RSC Adv. 6 (2016) 24645–24650.
- [41] W. Wang, J. Zhang, S. Yang, B. Ding, X. Song, ChemSusChem 6 (2013) 1945–1952.
- [42] D. Chen, C. Li, H. Liu, F. Ye, J. Yang, Sci. Rep. 5 (2015) 11949–11957.
- [43] J. Xu, T. White, P. Li, C.H. He, J.G. Yu, W.K. Yuan, Y.F. Han, J. Am. Chem. Soc. 132 (2010) 10398–10406.
- [44] J.-J. Feng, S.-S. Chen, X.-L. Chen, X.-F. Zhang, A.-J. Wang, J. Colloid Interface Sci. 509 (2018) 73–81.
- [45] J.-N. Zheng, S.-S. Li, X. Ma, F.-Y. Chen, A.-J. Wang, J.-R. Chen, J.-J. Feng, J. Power Sources 262 (2014) 270–278.
- [46] D. Kaplan, L. Burstein, Y. Rosenberg, E. Peled, J. Power Sources 196 (2011) 8286–8292.
- [47] X. Zhang, H. Wang, J. Key, V. Linkov, S. Ji, X. Wang, Z. Lei, R. Wang, J. Electrochem. Soc. 159 (2012) 270–276.
- [48] N.M. Sánchez-Padilla, S.M. Montemayor, L.A. Torres, F.J.R. Varela, Int. J. Hydrogen Energy 38 (2013) 12681–12688.
- [49] R. Wang, H. Li, H. Feng, H. Wang, Z. Lei, J. Power Sources 195 (2010) 1099–1102.
- [50] H. Gao, S. Liao, J. Zeng, Y. Xie, D. Dang, Electrochim. Acta 56 (2011) 2024–2030.
- [51] J.R. Kitchin, J.K. Nørskov, M.A. Barteau, J.G. Chen, J. Chem. Phys. 120 (2004) 10240–10246.
- [52] A. Groß, Top. Catal. 37 (2006) 29–39.
- [53] F.A. Al-Odail, A. Anastasopoulos, B.E. Hayden, Phys. Chem. Chem. Phys. 12 (2010) 11398–11406.
- [54] B.D. Cullity, S.R. Stock, Elements of X-ray Diffraction, Pearson, London, 2014, pp. 414–416.
- [55] A. Weibel, R. Bouchet, F. Boulc', P. Knauth, Chem. Mater. 17 (2005) 2378–2385.
- [56] G. Darabdhara, M.A. Amin, G.A.M. Mersal, E.M. Ahmed, M.R. Das, M.B. Zakaria, V. Malgras, S.M. Alshehri, Y. Yamauchi, S. Szuneritsj, R. Boukherroub, J. Mater. Chem. A Mater. Energy Sustain. 3 (2015) 20254–20266.
- [57] N. Gerales, D.F. Silva, E.S. Pino, J.C.M. Silva, R.F.B. Souza, P. Hammer, E.V. Spinace, A.O. Neto, M. Linardi, M.C. Santos, Electrochim. Acta 111 (2013) 455–465.
- [58] Z. Zhang, L. Xin, J. Qi, D.J. Chadderton, W. Li, Appl. Catal. B 136–137 (2013) 29–39.
- [59] Z.-H. Liu, Y.-Y. Feng, Y. Xu, P. Wang, W.-H. Wang, D.-S. Kong, J. Power Sources 232 (2013) 99–105.
- [60] C.-W. Yi, K. Luo, T. Wei, D.W. Goodman, J. Phys. Chem. B 109 (2005) 18535–18540.
- [61] D.A.J. Rand, R. Woods, J. Electroanal. Chem. 36 (1972) 57–69.
- [62] P.-P. Fang, A. Jutand, Z.-Q. Tian, C. Amatore, Angew. Chem. 123 (2011) 12392–12396.
- [63] Y.W. Lee, M. Kim, Y. Kim, S.W. Kang, J.-H. Lee, S.W. Han, J. Phys. Chem. C 114 (2010) 7689–7693.
- [64] M. Simões, S. Baranton, C. Coutanceau, Appl. Catal. B 93 (2010) 354–362.
- [65] M.M. Jaksic, B. Johansen, R. Tunold, Int. J. Hydrogen Energy 18 (1993) 111–124.
- [66] M. Łukaszewski, A. Czerwinski, J. Alloys. Compd. 473 (2009) 220–226.
- [67] C. Guofeng, S. Shuqin, S.P. Kang, K. Andrzej, B. Claudio, J. Phys. Chem. C 113 (2009) 15639–15642.
- [68] Q. Dong, Y. Zhao, X. Han, Y. Wang, M. Liu, Y. Li, Int. J. Hydrogen Energy 39 (2014) 14669–14679.
- [69] A.N. Gerales, D.F. Silva, J.C.M. Silva, R.F.B. Souza, E.V. Spinacé, A.O. Neto, M. Linardi, M.C. Santos, J. Braz. Chem. Soc. 25 (2014) 831–840.
- [70] Q. Wang, X. Cui, W. Guan, X. Zhang, C. Liu, T. Xue, H. Wang, W. Zheng, Microchim. Acta 181 (2014) 373–380.
- [71] M. Watanabe, S. Motoo, J. Electroanal. Chem. 60 (1975) 259–266.
- [72] B. Beden, A. Cetin, A. Kahyaoglu, D. Takky, C. Lamy, J. Catal. 104 (1987) 37–46.
- [73] A. Roudgar, Groß A, Surf. Sci. 597 (2005) 42–50.
- [74] F. Gao, D.W. Goodman, Chem. Soc. Rev. 41 (2012) 8009–8020.
- [75] A. Roudgar, Groß A, J. Electroanal. Chem. 548 (2003) 121–130.
- [76] J.-H. Koh, R. Abbaraju, P. Parthasarathy, A.V. Virkar, J. Power Sources 261 (2014) 271–277.
- [77] M.M.O. Thotiyil, T.R. Kumar, S. Sampath, J. Phys. Chem. C 114 (2010) 17934–17941.
- [78] X. Fang, L. Wang, P.K. Shen, G. Cui, C. Bianchini, J. Power Source 195 (2010) 1375–1378.
- [79] M. Nie, P.K. Shen, Z.D. Wei, J. Power Sources 167 (2007) 69–73.
- [80] V. Bambagioni, C. Bianchini, J. Filippi, A. Marchionni, F. Vizza, P. Bert, A. Tampucci, Electrochem. Commun. 11 (2009) 1077–1080.
- [81] H. Chaijen, H. Chienwen, H. Yaowu, L. Fuqiang, Electrochem. Commun. 23 (2012) 133–136.
- [82] M. Heggen, M. Oezaslan, L. Houben, P. Strasser, J. Phys. Chem. 116 (2012) 19073–19083.
- [83] Y.-X. Jiang, S.-G. Sun, N. Ding, Chem. Phys. Letters 344 (2001) 463–470.